inorganics

MDPI

Article

Ba_5Sb_8: The Highest Homologue of the Family of Binary Semiconducting Barium Antimonides Ba_nSb_{2n-2} ($n \geq 2$)

S. M. Gayomi K. Samarakoon [1], Alexander Ovchinnikov [2], Sviatoslav Baranets [1,*] and Svilen Bobev [2,*]

[1] Department of Chemistry, Louisiana State University, Baton Rouge, Baton Rouge, LA 70803, USA; ssamar4@lsu.edu
[2] Department of Chemistry and Biochemistry, University of Delaware, Newark, DE 19716, USA; alexovc@udel.edu
* Correspondence: sbaranets@lsu.edu (S.B.); bobev@udel.edu (S.B.)

Abstract: A novel binary compound within the Ba–Sb phase diagram, Ba_5Sb_8, was synthesized by combining elements with an excess of Sb in an alumina crucible. Structural elucidation was performed using single-crystal X-ray diffraction. This compound crystallizes in the orthorhombic space group *Fdd*2 with unit cell parameters of a = 15.6568(13) Å, b = 35.240(3) Å, c = 6.8189(6) Å, adopting its own structure type. The most distinctive features of the structure are the eight-membered $[Sb_8]^{10-}$ polyanionic fragments which have no known precedents among antimonides. They are separated by five Ba^{2+} cations, which afford the charge balance and enable adherence to the Zintl–Klemm formalism. Ba_5Sb_8 is the highest known member of the homologous series within the family of barium antimonides Ba_nSb_{2n-2} ($n \geq 2$), all of which boast anionic substructures with oligomeric moieties of pnictogen atoms with varied lengths and topologies. Electronic structure calculations indicate an indirect narrow bandgap of ca. 0.45 eV, which corroborates the valence-precise chemical bonding in Ba_5Sb_8.

Keywords: Zintl phases; solid-state synthesis; semiconductors; crystal structure; pnictides

check for updates

Citation: Samarakoon, S.M.G.K.; Ovchinnikov, A.; Baranets, S.; Bobev, S. Ba_5Sb_8: The Highest Homologue of the Family of Binary Semiconducting Barium Antimonides Ba_nSb_{2n-2} ($n \geq 2$). *Inorganics* **2024**, *12*, 3. https://doi.org/10.3390/inorganics12010003

Academic Editors: Christian M. Julien, Guido Kickelbick, Alexander S. Novikov, Gary Hix and Hans-Conrad zur Loye

Received: 13 November 2023
Revised: 8 December 2023
Accepted: 11 December 2023
Published: 20 December 2023

Copyright: © 2023 by the authors. Licensee MDPI, Basel, Switzerland. This article is an open access article distributed under the terms and conditions of the Creative Commons Attribution (CC BY) license (https://creativecommons.org/licenses/by/4.0/).

1. Introduction

Discovering novel compounds and investigating their structure–property relationships stands as a pivotal pursuit in the field of solid-state chemistry and material science. Within this domain, Zintl phases have emerged as a fascinating class of polar intermetallic compounds, gathering significant attention for their wide range of structural and electronic properties [1]. These compounds bear the namesake of Eduard Zintl, who was a progenitor of their study in the first quarter of the 20th century, focusing on binary phases composed of the alkali or alkaline-earth metals in conjunction with main group metalloids [2].

In general terms, the chemical bonding in Zintl phases adheres to the basic valence principles. As such, their structures include (i) an ionic component involving electropositive cations donating their electrons to the more electronegative elements and (ii) a covalent component within polyanionic frameworks or clusters composed by these electronegative elements [2]. Remarkably, the applicability of the Zintl concept allows for the creation of a broad spectrum of semiconducting materials with potential for applications in (i) thermoelectric technology, primarily due to the excellent tunability of transport properties [3], (ii) catalysis, even in the absence of the transition metals [4], (iii) photovoltaics [5], energy storage [6], and those with topological insulating properties [7]. Many Zintl phases are environmentally friendly and sustainable materials. They can be composed of earth-abundant elements, reducing reliance on rare or toxic elements, which is especially important for the development of clean energy technologies.

The majority of the recently discovered Zintl phases are represented by complex ternary and quaternary compounds [8,9], although novel binary phases akin to those studied by Zintl are also occasionally identified [10–12]. Research efforts are primarily focused

on Zintl pnictides, which are characterized by diverse anionic substructures primarily due to the ability of pnictogens (Pn = P, As, Sb, Bi) to form homoatomic bonds. It results in enormous compositional and structural abundance among binary and multinary Zintl compounds. For instance, there are almost a dozen binary phases known in the Ba–Sb phase diagram. Examples include Ba_2Sb_3 [13], Ba_5Sb_4 [14], $Ba_{11}Sb_{10}$ [15], $BaSb_2$ [16], and $BaSb_3$ [17], to name a few. Recently, we reported a detailed crystal structure description of yet another binary Zintl phase, $Ba_{16}Sb_{11}$, which has been shown to crystallize in two polymorphic modifications [11]. Over the course of those studies, we have discovered a hitherto unknown Ba_5Sb_8 Zintl phase. This work will comprehensively detail the synthesis process, provide insights into the bonding and structural details, and elucidate the electronic structure of this unique compound, thus contributing to the development of Zintl chemistry.

2. Results and Discussion

2.1. Synthesis

The initial experiment that allowed for the serendipitous discovery of Ba_5Sb_8 was designed with the aim to explore the Ba–Cr–Sb system for possible ternary compounds. Prior synthetic efforts with early transition elements, such as Ti and V, yielded several novel pnictides [18,19]. Thus, the progression from Group 4 and Group 5 elements to Group 6 elements constituted a logical extension of our experiments, particularly in light of the high solubility of Cr in excess of Sb at high temperatures and the existence of binary chromium antimonides, such as CrSb and $CrSb_2$. However, to date, at the reaction conditions that were employed, we did not observe the formation of ternary compounds. Instead, among the multiple binary reaction products, single crystals of CrSb and the title Ba_5Sb_8 compound were most frequently encountered.

Another noteworthy observation pertains to the essential role of chromium in the synthesis of the Ba_5Sb_8 phase. To elucidate this phenomenon, we performed a series of parallel experiments that maintained the same nominal Ba:Sb stoichiometry but excluded Cr from the reaction mixture. These reactions were run at the same temperatures as before; they exclusively yielded known antimony-rich binary barium antimonides, namely $BaSb_2$ and $BaSb_3$, further affirming the necessity of Cr in the synthesis process. We speculate that Cr may play a "catalytic" role of some kind, similar to what Ge does for the synthesis of the $Yb_5Al_2Sb_6$ compound or Bi does in the synthesis of recently reported P_{11} allotrope [20,21]. We also note that all reactions were readily reproducible when employing starting materials from various commercial suppliers.

SCXRD studies (vide infra) of the title phase indicate an unambiguous structure solution with all atomic sites exhibiting full occupancy, thus indicating the absence of Cr in the crystal structure of Ba_5Sb_8. Semiquantitative elemental microanalysis of the single crystal used in the SCXRD studies, performed with the aid of SEM-EDS electron microscopy, also indicated the absence of foreign elements and confirmed the presence of Ba and Sb in a 5:8 ratio. The exact role of Cr in the synthetic process remains unclear, yet its presence is established as a prerequisite for the formation of the Ba_5Sb_8 phase.

2.2. Crystal Structure and Structural Relationships

Among the Zintl pnictides, compounds of the "5–8" variety are not widely recognized with only very few reported to date. These are the Zintl phases Ca_5P_8 [22] and Cs_5Sb_8 [23] and a series of intermetallic compounds with the $(Ti,Zr)_5Sb_8$ structure type [24,25]. However, their crystal structures are distinct from the one reported herein, and their brief schemes are provided in Appendix A.

The comprehensive crystallographic analysis of the Ba_5Sb_8 structure reveals a great degree of complexity (Figure 1). It is an orthorhombic, non-centrosymmetric structure with the space group *Fdd*2 (no. 43) with a relatively large unit cell volume (Table 1). There are three crystallographically independent Ba sites and four Sb sites occupying general positions with the exception of Ba3 (Table 2), yielding the Wyckoff sequence b^6a. There are

no precedents for such a structure in the ICSD database; therefore, it ought to constitute a new structure type with the Pearson symbol *oF*104.

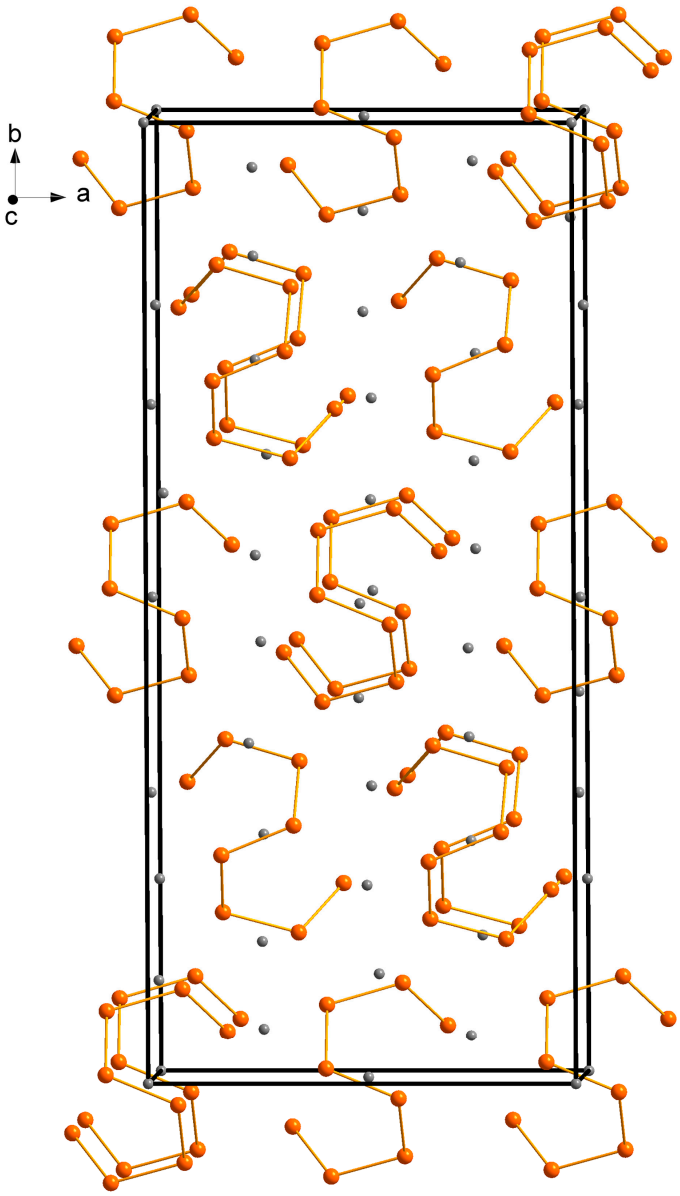


Figure 1. A schematic representation of the Ba_5Sb_8 unit cell, emphasizing the eight-membered oligomeric fragments made of Sb atoms. Barium atoms are shown in gray, and antimony atoms are shown in orange. The unit cell is outlined.

Table 1. Selected data collection details and crystallographic data for Ba_5Sb_8 (T = 100 K; Mo Kα, λ = 0.71073 Å; Z = 8).

Chemical Formula	**Ba_5Sb_8**
fw/g mol^{-1}	1660.70
Space group	*Fdd*2
a/Å	15.6568(13)
b/Å	35.240(3)
c/Å	6.8189(4)
V/Å^3	3762.3
$\rho_{calc.}$/g cm^{-3}	5.86

Table 1. *Cont.*

Chemical Formula	Ba_5Sb_8
μ (Mo-Kα)/cm^{-1}	215.2
Reflections collected/Independent reflections	10675/2811
R_1 (I > 2$\sigma_{(I)}$) [a]	0.0204
wR_2 (I > 2$\sigma_{(I)}$) [a]	0.0418
R_1 (all data) [a]	0.0209
wR_2 (all data) [a]	0.0419
$\Delta\rho_{max,min}$/e^{-}·Å^{-3}	1.67, −1.01
CCDC deposition number	2307632

[a] $R_1 = \Sigma||F_o| - |F_c||/\Sigma|F_o|$; $wR_2 = [\Sigma[w(F_o^2 - F_c^2)^2]/[\Sigma w(F_o^2)^2]]^{1/2}$, where $w = 1/[\sigma^2 F_o^2 + (0.0132{\cdot}P)^2 + (106.0190{\cdot}P)]$, and $P = (F_o^2 + 2F_c^2)/3$.

Table 2. Refined atomic coordinates and equivalent isotropic displacement parameters (U_{eq} [a], Å^2) for Ba_5Sb_8.

Atom	Site	*x*	*y*	*z*	U_{eq}
Ba1	16*b*	0.0017(1)	0.2017(1)	0.1058(1)	0.007(1)
Ba2	16*b*	0.5149(1)	0.1031(1)	0.1323(1)	0.006(1)
Ba3	8*a*	0	0	0.0000(1)	0.006(1)
Sb1	16*b*	0.0679(1)	0.3027(1)	0.1182(1)	0.007(1)
Sb2	16*b*	0.0846(1)	0.1005(1)	0.1286(1)	0.007(1)
Sb3	16*b*	0.1598(1)	0.1714(1)	0.4507(1)	0.007(1)
Sb4	16*b*	0.6654(1)	0.2346(1)	0.2396(1)	0.007(1)

[a] U_{eq} is defined as one-third of the trace of the orthogonalized U_{ij} tensor.

All Ba atoms are eight coordinated by Sb atoms with observed interatomic Ba–Sb distances in the ranges of 3.50–3.80 Å for Ba1, 3.48–3.67 Å for Ba2, and 3.40–3.76 Å for Ba3. These values are close to the sum of the covalent radii of Ba and Sb 3.50(16) and are typically observed in multiple Zintl antimonides [26]. Ba atoms are arranged in a framework composed of layers of alternating perpendicularly oriented distorted trigonal prisms stacked along the a-axis (Figure 2). These prisms host the Sb atoms composing the $[Sb_8]^{10-}$ complex Zintl anion, which is discussed in detail below.

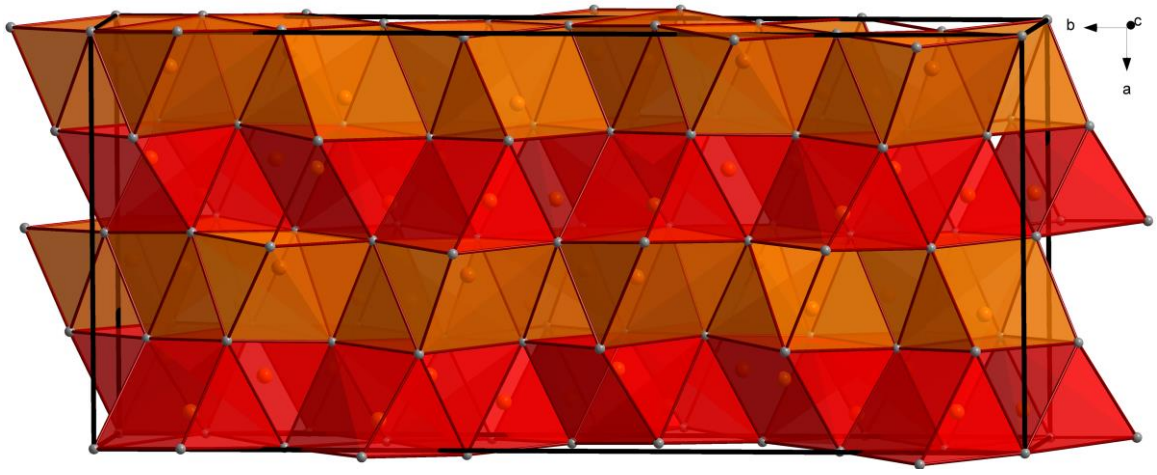


Figure 2. The sequence of alternating layers composed of perpendicularly oriented distorted trigonal prisms made of Ba atoms along the a-axis. Sb atoms are packed inside the Ba atom framework. The color code is the same as in Figure 1. Alternating slabs of perpendicular Ba_6 prisms are denoted in red and orange. The unit cell is outlined.

A detailed description of bonding within these Sb-centered polyhedra is needed for the proper understanding of the $[Sb_8]^{10-}$ polyanion, in which Sb atoms exhibit two types of coordination environments. Sb1 and Sb2 atoms can be viewed as six-coordinated by Ba atoms in a distorted trigonal-prismatic fashion (Figure 3c,d). Sb–Ba interatomic distances fall down in the ranges of 3.50–3.71 Å and 3.55–3.88 Å for $[Sb_1Ba_6]$ and $[Sb_2Ba_6]$ prisms, respectively. These two prisms are face-sharing and allow for the existence of Sb_1–Sb_2 contact of 2.86 Å with Sb atoms located almost in the center of each polyhedron. Sb3 and Sb4 atoms are also located within the framework of Ba prisms, although the positions of both Sb atoms are noticeably off-centered and significantly shifted toward the face of $[SbBa_6]$ polyhedra, so the Sb atoms are only slightly protruding over the face plane made of Ba atoms (Figure 3e,f). Sb–Ba interatomic distances in such a distorted square-planar environment of $[Sb_3Ba_4]$ and $[Sb_4Ba_4]$ range from 3.39 to 3.57 Å and from 3.56 to 3.76 Å, whereas complementary contacts that are needed to complete the polyhedra are longer than 4 Å, being beyond the bonding range.

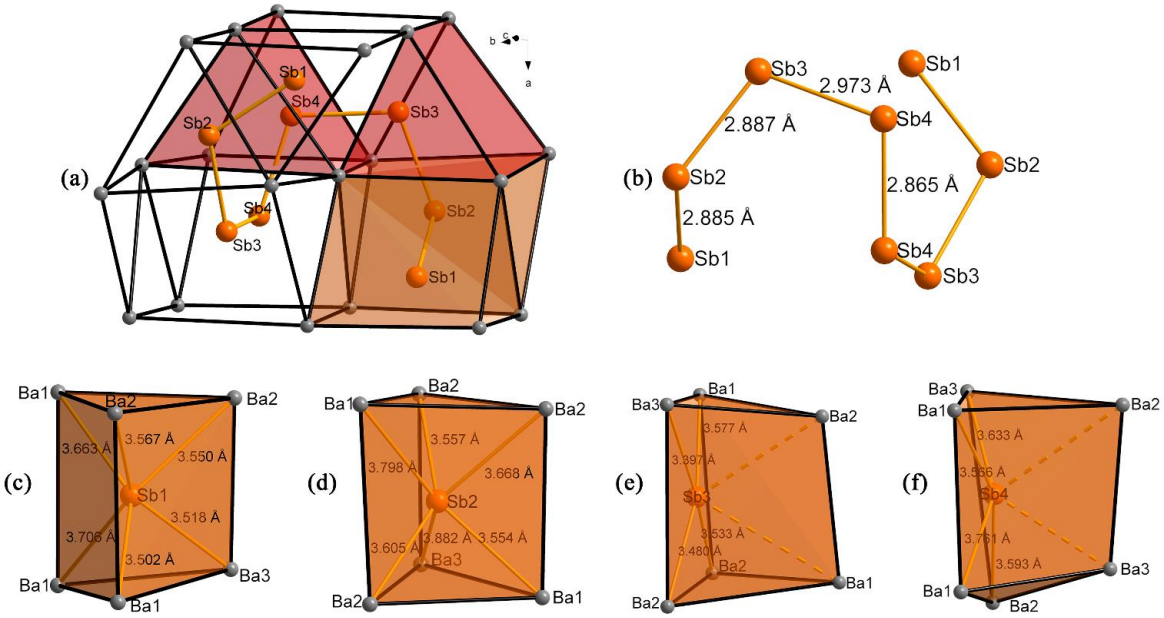


Figure 3. (**a**) The trigonal prismatic arrangement of Sb-centered $[SbBa_6]$ and empty $[Ba_6]$ polyhedra encasing the $[Sb_8]^{10-}$ polyanion; (**b**) close-up view of the $[Sb_8]^{10-}$ chain-like Zintl anion supplemented with the respective Sb–Sb distances; (**c**–**f**) distinct representation of Sb-centered trigonal prisms of Ba atoms. Sb_1 and Sb_2 atoms are located close to the center of the prisms, whereas Sb3 and Sb4 atoms are closer to one of the rectangular faces.

The $[Sb_3Ba_4]$ distorted square plane can be viewed as a continuation of the face that belongs to $[Sb_1Ba_6]$ trigonal prisms, whereas $[Sb_4Ba_4]$ plane complements the shared face of $[Sb_1Ba_6]$ and $[Sb_2Ba_6]$ prisms and together with the $[Sb_3Ba_4]$ plane completes another prism yet without the Sb atom. This "empty" prism is enclosed between $[Sb_1Ba_6]$ and $[Sb_2Ba_6]$ polyhedra by sharing bases (Figure 3a). Since the Sb_3 atom is only 0.35 Å away from the shared face with the $[Sb_2Ba_6]$ prism, this allows for the realization of Sb2–Sb3 contact of 2.89 Å.

Structural differences between Sb-centered polyhedra can be better understood by analyzing the hallmark of the Ba_5Sb_8 crystal structure—the unique $[Sb_8]^{10-}$ Zintl anion (Figure 3b). The whole crystal structure of Ba_5Sb_8 can be viewed as a complex arrangement of these asymmetric anionic units, which are kept separated by the Ba^{2+} cations (Figure 1). These eight-membered fragments are characterized by distinct handedness and are stacked along the b-axis in an alternating checkerboard-like pattern, as illustrated in Figure 2. The $[Sb_8]^{10-}$ chain is composed of eight Sb atoms in the [Sb1–Sb2–Sb3–Sb4–Sb4–Sb3–Sb2–Sb1] fashion (Figure 3b). The unit has a C_2 rotational axis of symmetry in a direction perpendic-

ular to the center of the Sb4–Sb4 bond and parallel to the c-axis. Bond lengths between Sb atoms are relatively uniform and fall in the range of 2.87–2.97 Å, being comparable to the most known barium Zintl antimonides [13,16] with the outlier value of 2.97 Å for Sb3–Sb4 contact. This bonding "anomaly" is well explained by the fact that Sb3- and Sb4-centered prisms do not share edges or faces but are separated by the "empty" interstitial trigonal prism composed of Ba atoms mentioned above. Noteworthy, such an interatomic distance was observed for Sb–Sb contact in the recently reported $Ba_{16}Sb_{11}$ phase [11]. $[Sb_3Ba_4]$ and $[Sb_4Ba_4]$ planes are also considered as faces of this interstitial prism in which Sb_3 and Sb_4 atoms protrude outward on 0.35 Å and 0.67 Å, respectively (Figure 3e,d).

All eight $[SbBa_6]$ prisms surrounding Sb atoms in the $[Sb_8]^{10-}$ unit are oriented in two perpendicular directions (Figure 3a). Two adjacent parallel polyhedra $[Sb1Ba_6]^{\cdot}$ and $[Sb_2Ba_6]^{\cdot}$ are followed by perpendicularly oriented $[Sb_3Ba_6]^{\cdot}$, "empty" $[Ba_6]^{\cdot}$, and $[Sb_4Ba_6]^{\cdot}$ prisms completing the first half ($^{\cdot}$) of the $[Sb_8]^{10-}$ unit. $[Sb4Ba_6]^{\cdot}$ polyhedra is face shared with the identical $[Sb4Ba_6]^{\cdot}$* prism from the second half ($^{\cdot}$*) of the $[Sb_8]^{10-}$ unit in a perpendicular manner so that the bases of the $[Sb_4Ba_6]^{\cdot}$* and $[Sb_2Ba_6]^{\cdot}$* prims are shared. The remaining polyhedra are symmetric, as was mentioned before, and the overall sequence can be described as follows: $\{[Sb_1Ba_6]^{\cdot}\uparrow-[Sb_2Ba_6]^{\cdot}\uparrow-[Sb_3Ba_6]^{\cdot}\rightarrow-[Ba_6]^{\cdot}\rightarrow -[Sb_4Ba_6]^{\cdot}\rightarrow-[Sb_4Ba_6]^{\cdot}*\uparrow-[Ba_6]^{\cdot}*\uparrow-[Sb_3Ba_6]^{\cdot}*\uparrow-[Sb_2Ba_6]^{\cdot}*\rightarrow-[Sb_1Ba_6]^{\cdot}*\rightarrow\}$, where arrows denote parallel (↑) and perpendicularly (→) oriented polyhedra. Consequently, $[Sb_2Ba_6]^{\cdot}$* and $[Sb_4Ba_6]^{\cdot}$ prisms share the base, too.

To our knowledge, the $[Sb_8]^{10-}$ complex polyanionic fragment (Figure 4a) has only one isosteric/isoelectronic analog previously reported within the realm of alkaline/rare-earth Zintl pnictides [8,27,28]. This isostructural $[As_8]^{10-}$ oligomer was observed alongside the $[As_4]^{6-}$ unit in the Ca_2As_3 structure, which should be more conveniently represented as $Ca_8As_{12} = (Ca^{2+})_8[As_8]^{10-}[As_4]^{6-}$ [28]. Ba_5Sb_8 remains the first antimonide with such an $[Sb_8]^{10-}$ eight-membered oligomeric unit. Among the other reported antimonides, the closest structural analog is Ba_2Sb_3, which can be re-written as Ba_4Sb_6 [13], because its anionic substructure consists of $[Sb_6]^{8-}$ oligomers composed of six independent Sb atoms (Figure 4b). Ba_4Sb_6 [13] belongs to the homologous series of Zintl antimonide, as discussed below. While the $[Sb_6]^{8-}$ unit can be viewed as a two-atoms shorter version of $[Sb_8]^{10-}$, their structures are noticeably distinct. Thus, the Sb_3–Sb_4–Sb_4–Sb_3 torsion angle with a central Sb_4–Sb_4 bond in Ba_5Sb_8 is close to the right angle (ca. 91.6°), while the analogous Sb_2–Sb_3–Sb_4–Sb_6 angle, with a central Sb_3–Sb_4 bond, is only ca. 10.2°, indicating different bond orientation for these two ions. The crystal structure of Ba_2Sb_3 is described in another article [13], whereas the detailed analysis of the electronic structure and properties of Ba_2Sb_3 as well as its yet-to-be-reported polymorph will be discussed in one of our future works.

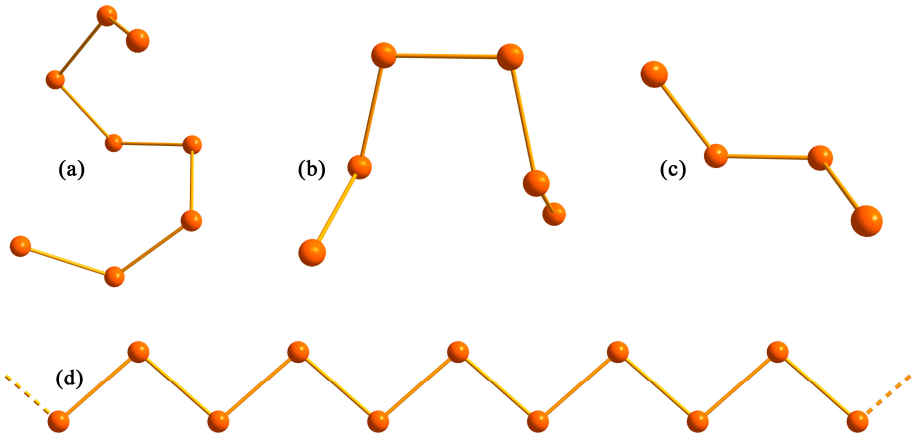


Figure 4. (**a**) Structural representation of the Sb_8 and As_8 polyanions observed in the structures of Ba_5Sb_8 and Ca_2As_3 (**a**); Sb_6 fragment observed in the structure of Ba_2Sb_3 (**b**); As_4 anion observed in the structure of Eu_3As_4 and Ca_2As_3 (**c**); and an infinite zig-zag Sb_∞ chain observed in the structure of $BaSb_2$ (**d**).

Given the presence of eight-membered and six-membered fragments of chains in this and other barium antimonides, we want to expand on the possibility that there are other compounds awaiting their discovery. This notion can be expressed in terms of a homologous series of binary compounds that differ by one $BaSb_2$ formula unit; i.e., all members of the family can be described in terms of Ba_nSb_{2n-2}. Within this formalism, the simplest member will be BaSb, or rather Ba_2Sb_2 (n = 2) featuring just simple dumbbells, $[Sb_2]^{4-}$, and the end member for $n = \infty$ will be $BaSb_2$, featuring infinite chains, formally $[Sb_2]^{2-}$ (Figure 4d). The highest homologue, which is represented by a finite number, is the title compound Ba_5Sb_8 (n = 5). Next in the series (in decreasing order, n = 4) is Ba_4Sb_6 (=Ba_2Sb_3), which was discussed above. Cutting one more $BaSb_2$ formula unit leads to Ba_3Sb_4, n = 3, whose structure is predicted to have $[Sb_4]^{6-}$ tetramers. Interestingly, while not all of these are experimentally confirmed to exist as barium antimonides, they are all known for other rare-earth or alkaline-earth metal pnictides. For example, "3–4" pnictides with four-membered Pn_4-polyanions are represented by multiple compositions belonging to the Eu_3As_4 structure type (Figure 4c) or a single representative of Ca_2As_3, as discussed above [28,29]. The only known barium-bearing representative is Ba_3P_4 [30], which exhibits a symmetric P_4 chain similar in configuration to the middle part of the Sb_8 fragment in Ba_5Sb_8, exposing a P1–P2–P2–P1 angle of 86.4°. The "1–1" or rather "2–2" composition of the Na_2O_2 structure type with Pn–Pn dumbbells is well known for multiple Zintl pnictides, although there are also no experimental reports on barium-bearing phases. Noteworthy, the existence and stability of both compositions, Ba_3Sb_4 and Ba_2Sb_2, has been theoretically predicted [31,32], and we speculate that extensive synthetic efforts will result in the successful synthesis of these homologs. Structures with Sb_{10} or Sb_{12} oligomeric units can only be discussed as a speculation at this point, since there are no known reported analogs or even theoretical predictions. It is acknowledged that the energy landscape will likely be riddled with shallow minima, and that Ba_6Sb_{10} and Ba_7Sb_{14} hypothetical compounds will be very challenging to isolate from the "thermodynamic" most-stable phases that are compositionally very close, i.e., $BaSb_2$ [16]. Alternative syntheses methods, not just a direct fusion of elements, are likely needed to afford the crystallization of the speculated phases.

2.3. Electronic Structure, Chemical Bonding, and Electron Count Considerations

Detailed structural analysis (vide supra) provided valuable insights into the chemical bonding, which laid the groundwork for the study of the electronic structure of Ba_5Sb_8. As previously mentioned, this phase belongs to the charge-balanced Zintl phases, maintaining a precise valence electron count according to the partitioning scheme $[(Ba^{2+})_5]^{10+}[(1b\text{-}Sb^{2-})_2(2b\text{-}Sb^{1-})_6]^{10-}$. Here, Sb atoms with a one-covalent bond (1*b*) or two-covalent bond (2*b*) are differentiated with formal charges Sb^{2-} and Sb^{1-}, respectively. Recall that within the Sb_8 fragment, there are two terminal Sb atoms, which are 1*b* and the six interior Sb atoms, which are 2*b*; they clearly must have different requirements as to how their octets will be completed.

While the Zintl–Klemm formalism and considerations of electronegativity differences between Ba and Sb offer an empirical understanding of the bonding situation and predict semiconducting behavior [33], a more comprehensive insight into the electronic structure of the title compound was gained through our calculations. The results of the electronic structure calculations for Ba_5Sb_8 are presented in Figures 5–7. According to Figure 5, the title phase is a semiconductor with a narrow, indirect bandgap of 0.45 eV. This value is in the range observed for multiple other Zintl antimonides, some of which are being tested for high-temperature thermoelectric energy conversion [34–38].

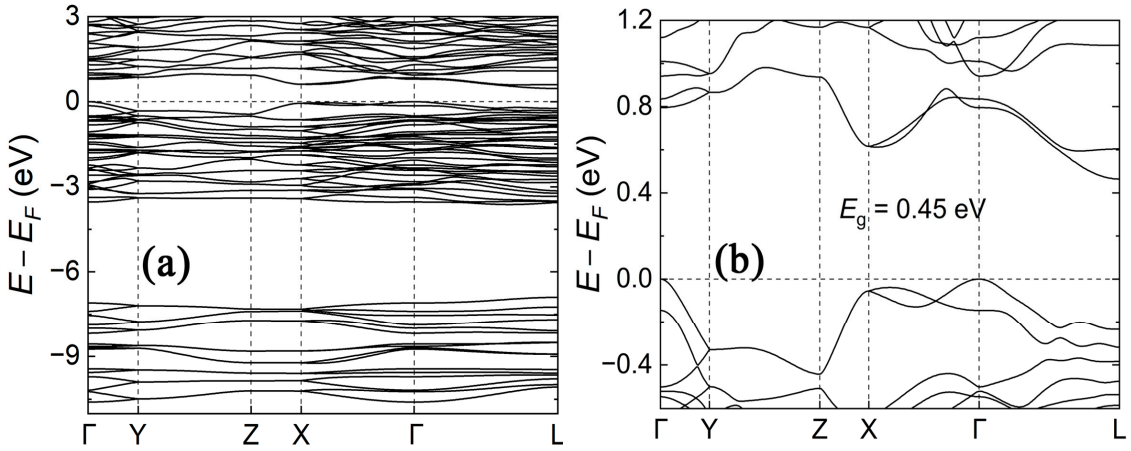


Figure 5. (**a**) Calculated bulk electronic band structure of Ba_5Sb_8 along high symmetry directions. (**b**) Zoomed-in view for the electronic band structure near the Fermi level, which reveals the indirect bandgap opening along the Γ and L points. The Fermi level is set at 0 eV.

Density of states (DOS) curves are presented in Figure 6. The total (TDOS) and partial (PDOS) exhibit features are already observed in other Zintl antimonides, $Ba_{16}Sb_{11}$, in particular [11]. The largest contributors to the total DOS between −10.5 and −7.1 eV are Sb orbitals; the area close to the valence band maxima (VBM) in the region above −3.9 eV is also mainly contributed by Sb orbitals. The states that will be more crucial in influencing the electronic transport in Ba_5Sb_8 are those that are located in close vicinity of the Fermi level and are contributed by both Ba and Sb orbitals. This is indicative of their participation in Ba–Sb bonding, which is not entirely ionic in nature. In particular, the greater involvement of empty Ba-d orbitals shows that Ba atoms are not just electron donors. The involvement of Ba in covalent-like chemical bonding signals a deviation from the classic ionic approximation. This suggests that the pure Zintl reasoning that will treat the Ba atoms merely as a space-filling cation and electron donor does not fully capture the nature of the chemical bonding in this binary phase. Expectedly, a large contribution from empty Ba 5d orbitals dominate the region just above the Fermi level.

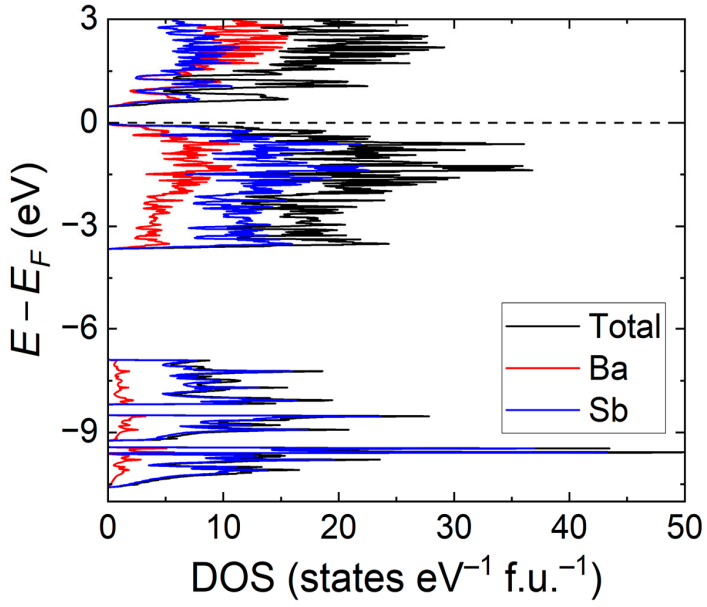


Figure 6. Density of states (DOS) of Ba_5Sb_8. The total (black trace) and projected density of states for the Ba and Sb contributions (red and blue traces, respectively). The Fermi level is taken as $E - E_F = 0$ eV.

To further elucidate the bonding situation for the Ba_5Sb_8 phase, we plot COHP curves for the average Ba–Sb and Sb–Sb bonds (Figure 7). As can be expected for Zintl antimonides, Ba–Sb bonds (considered within the range of 3.39 Å–3.88 Å) are optimized at the Fermi level. Averaged Sb–Sb contacts within the $[Sb_8]^{10-}$ unit are also optimized, although noticeable domains of antibonding character are observed near the VBM down to −1.5 eV. These features are typical for Zintl phases with homoatomic Sb–Sb bonds [11,37]. However, separate COHP curves for Sb1–Sb2, Sb2–Sb3, Sb3–Sb4, and Sb4–Sb4 show a distinct nonuniformity. While Sb1–Sb2, Sb2–Sb3, and Sb4–Sb4 readily follow the provided description, the COHP curve for the Sb3–Sb4 contact indicates the presence of bonding domains at the VBM. This is likely associated with the longest interatomic Sb3–Sb4 distance, which corroborates well with the crystallographic data presented in Table 2. COHP curves for the separate Ba–Sb contacts within the $[Sb_1Ba_6]$ prism are nearly identical, indicating distinct bonding between these two atoms. The longest Ba–Sb contacts within $[Sb_3Ba_6]$ and $[Sb_4Ba_6]$ prisms expectedly show large domains of antibonding character at the VBM.

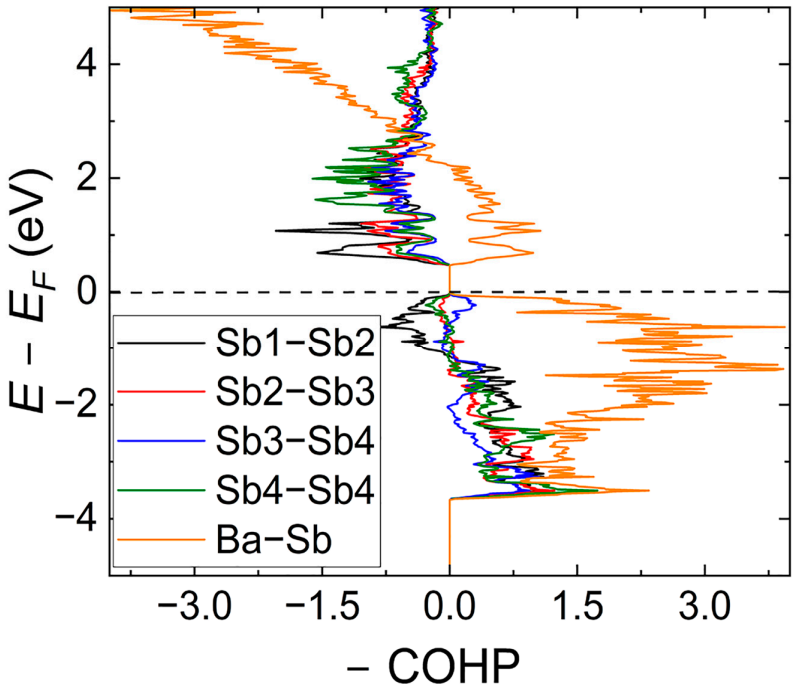


Figure 7. Calculated COHP curves for the average Ba–Sb and specific Sb–Sb interactions in the $[Sb_8]$ fragment.

To further elucidate these effects, we calculated –ICOHP values for the Ba–Sb and Sb–Sb contacts. The average –ICOHP for the Ba–Sb contact is ca. 0.65 eV/bond, whereas the calculated values for the Sb1–Sb2, Sb2–Sb3, Sb3–Sb4, and Sb4–Sb4 contacts were 1.91, 1.85, 1.35, and 2.02 eV/bond, respectively, indicating the stronger covalent character of the homoatomic Sb–Sb bond compared to Ba–Sb interactions. This corroborates well with the Zint–Klemm concept, where the covalently bonded anions accept electrons from the electropositive electron donor. The values of –ICOHP for Sb–Sb bonds are uniform with the exception of Sb3–Sb4 contact (which is of least antibonding character), which aligns closely with the longest interatomic distance for the latter (Table 3) and, therefore, weaker covalent interaction.

Table 3. Selected interatomic distances (Å) and bond angles (°) in Ba_5Sb_8.

Atom Pair	Distance/Å	Atom Pair	Distance/Å	Atoms Pair	Distance/Å
Ba1–Sb1	3.5021(9)	Ba2–Sb2	3.6054(8)	Sb1–Sb2	2.8855(7)
Ba1–Sb1	3.6631(9)	Ba2–Sb3	3.5326(7)	Sb2–Sb3	2.8868(8)
Ba1–Sb2	3.5538(7)	Ba2–Sb4	3.5929(8)	Sb3–Sb4	2.9728(8)
Ba1–Sb3	3.5772(7)	Ba3–Sb1	3.5185(6)	Sb4–Sb4	2.8655(11)
Ba1–Sb4	3.5663(8)	Ba3–Sb1	3.5185(6)	**Atoms**	**Angles/°**
Ba1–Sb1	3.7062(8)	Ba3–Sb2	3.8820(6)	Sb1–Sb2–Sb3	116.75(2)
Ba2–Sb1	3.5672(8)	Ba3–Sb3	3.3970(7)	Sb2–Sb3–Sb4	106.58(2)
Ba2–Sb1	3.5502(8)	Ba3–Sb4	3.7639(9)	Sb4–Sb4–Sb3	108.16(2)
Ba2–Sb2	3.6686(8)	Ba3–Sb4	3.6328(9)		

3. Materials and Methods

3.1. Synthesis

All synthetic and post-synthetic procedures were carried out within the atmosphere-controlled environment of an argon-filled glovebox or under vacuum to ensure the exclusion of moisture and oxygen. All reagents in the elemental form were sourced from Sigma-Aldrich or Thermo Fisher Scientific with a certified purity level of 99.2% wt. or higher. All starting materials were used as received without further purification.

Ba_5Sb_8 can be readily synthesized by employing a self-flux reaction with an excess of molten Sb. This method has been proven useful before and yielded several novel Zintl antimonides, such as CaV_3Sb_4 and $Ba_5V_{12}Sb_{19}$ [18,19]. Approximately 3.0 g of the elemental mixture in a predetermined stoichiometric ratio of Ba:Cr:Sb = 2:1:3 was loaded into an alumina crucible. Subsequently, it was placed inside a fused silica ampule, which was then evacuated and flame-sealed. The ampoule was then heated in a programmable furnace from 100 to 950 °C at a rate of 200 °C h^{-1} and allowed to homogenize at this temperature for 20 h, which was followed by slow cooling down to 750 °C at a rate of 5 °C h^{-1}. Upon reaching the target temperature of 750 °C, the reacted mixture was carefully extracted from the furnace, inverted, and spun in a centrifuge to separate Sb from the formed crystals. A relatively high centrifugation temperature was selected due to the high melting point of Sb, ca. 631 °C. After opening the ampule in the argon-filled glove box, a solid product consisting of flake-like, silver- and black-colored, air-sensitive crystals was found on the bottom of the crucible.

3.2. X-ray Diffraction Methods

Powder X-ray diffraction (PXRD) patterns were recorded in the reflection mode at room temperature using a Rigaku Miniflex 600 diffractometer (Rigaku Corp., Tokyo, Japan) (Cu Kα radiation, λ = 1.5406 Å, Ge monochromator). The PXRD data were acquired using a θ-θ step-scan mode with 0.05° increments and a 2 s collection period per step. However, during the extremely air- and moisture-sensitive nature of barium antimonides, including the title Ba_5Sb_8 compound, the measured powder pattern indicates a high degree of phase amorphization. For several samples, peaks of the stable CrSb binary phase were also identified.

The crystal structure of Ba_5Sb_8 was studied using the single-crystal X-ray diffraction (SCXRD) method. Data were collected on a Bruker *APEX II* CCD diffractometer (Bruker, Madison, WI, USA) equipped with a Mo Kα (λ = 0.71073 Å) radiation source under cryogenic conditions at 100(2) K in a cold nitrogen stream. Suitable single crystals were carefully selected, cut to the desired sizes of less than 100 μm, and affixed to MiTeGen plastic loops. Data integration and absorption correction were executed using the *SAINT* and *SADABS* programs, respectively, which were both integrated with the *APEX3* software package (v2019. 1–0) [39,40]. The crystal structure was initially solved using the intrinsic

phasing method using the *SHELXT* program and refined by the full-matrix least squares method on F^2 with *SHELXL* [41,42]. The Olex2 program package was used as a graphical interface [43]. Atomic coordinates were standardized by using the *STRUCTURE TIDY* program [44]. Tables 1–3 contain selected data collection and other crystallographic parameters of relevance.

3.3. Electronic Structure Calculations

Electronic structure calculations for Ba_5Sb_8 composition were performed using *TB-LMTO-ASA* code [45] within the von Barth–Hedin implementation of the local density approximation (LDA) functional theory [46]. Empty spheres were introduced to satisfy the atomic sphere approximation (ASA) using a built-in procedure in the code. The refined experimental unit cell parameters and atomic coordinates were employed for calculations (Table 1; Table 2). The basic set included Ba 5s, (6p), and 5d and Sb 5s, 5p, and 5(d) orbitals (the downfolded orbitals are in parentheses). After checking for convergence, the Brillouin zone was sampled using a $10 \times 10 \times 10$ k-point grid, which was followed by the calculation of the density of states (DOS) and chemical bonding analysis using the Crystal Orbital Hamilton Population (COHP) method as implemented in the *TB-LMTO-ASA* code [47]. The Fermi level was selected as the reference energy (E_F = 0 eV).

4. Conclusions

Ba_5Sb_8 adopts its own structure type, crystallizing in a non-centrosymmetric orthorhombic space group *Fdd*2. Its hallmark is the anionic substructure composed of a unique eight-membered anionic chain, which is denoted as $[Sb_8]^{10-}$. The presence of complex, covalently bonded polyanions with homoatomic Sb–Sb bonds that accept electrons from electropositive Ba cations allows Ba_5Sb_8 to be characterized within the Zint–Klemm formalism. The intrinsic semiconducting nature of this phase has been predicted through the charge partitioning, $(Ba^{2+})_5[Sb_8]^{10-}$, and electronic structure calculations. This novel compound belongs to the family of narrow bandgap materials with a calculated bandgap of 0.45 eV. The discovery of Ba_5Sb_8 Zintl antimonide enriches the Ba–Sb phase diagram and provides valuable insights into the existence of a homologous series of barium antimonides with the formula Ba_nSb_{2n-2}. The class of barium antimonides with Sb_n polyanions necessitates a comprehensive study of the compositional abundance and transport properties for the establishment of proper structure–property correlations.

Author Contributions: Methodology, A.O. and S.B. (Sviatoslav Baranets); investigation, A.O.; validation, S.M.G.K.S.; formal analysis, S.M.G.K.S. and S.B. (Sviatoslav Baranets); data curation, A.O. and S.M.G.K.S.; writing—original draft preparation, S.M.G.K.S.; visualization, S.M.G.K.S. and S.B. (Sviatoslav Baranets); conceptualization, writing—review and editing, supervision, project administration, funding acquisition, S.B. (Sviatoslav Baranets) and S.B. (Svilen Bobev) Authors have read and agreed to the published version of the manuscript. All authors have read and agreed to the published version of the manuscript.

Funding: Svilen Bobev acknowledges financial support from the United States Department of Energy, Office of Science, Basic Energy Sciences, under Award #DE-SC0008885. Sviatoslav Baranets acknowledges financial support (start-up funding) from the College of Science and Department of Chemistry at Louisiana State University.

Data Availability Statement: The corresponding crystallographic information file (CIF) has been deposited with the Cambridge Crystallographic Data Centre (CCDC) and can be obtained free of charge via visiting www.ccdc.cam.ac.uk/data_request/cif or calling The Cambridge Crystallographic Data Centre at 12 Union Road, Cambridge CB2 1EZ, U.K., +44-1223-336033. The correspondent depository number is 2307632.

Acknowledgments: Sviatoslav Baranets acknowledges the LSU Provost's Fund for Innovation in Research–Council on Research Summer Stipend Program for the Summer support.

Conflicts of Interest: The authors declare no conflict of interest.

Appendix A

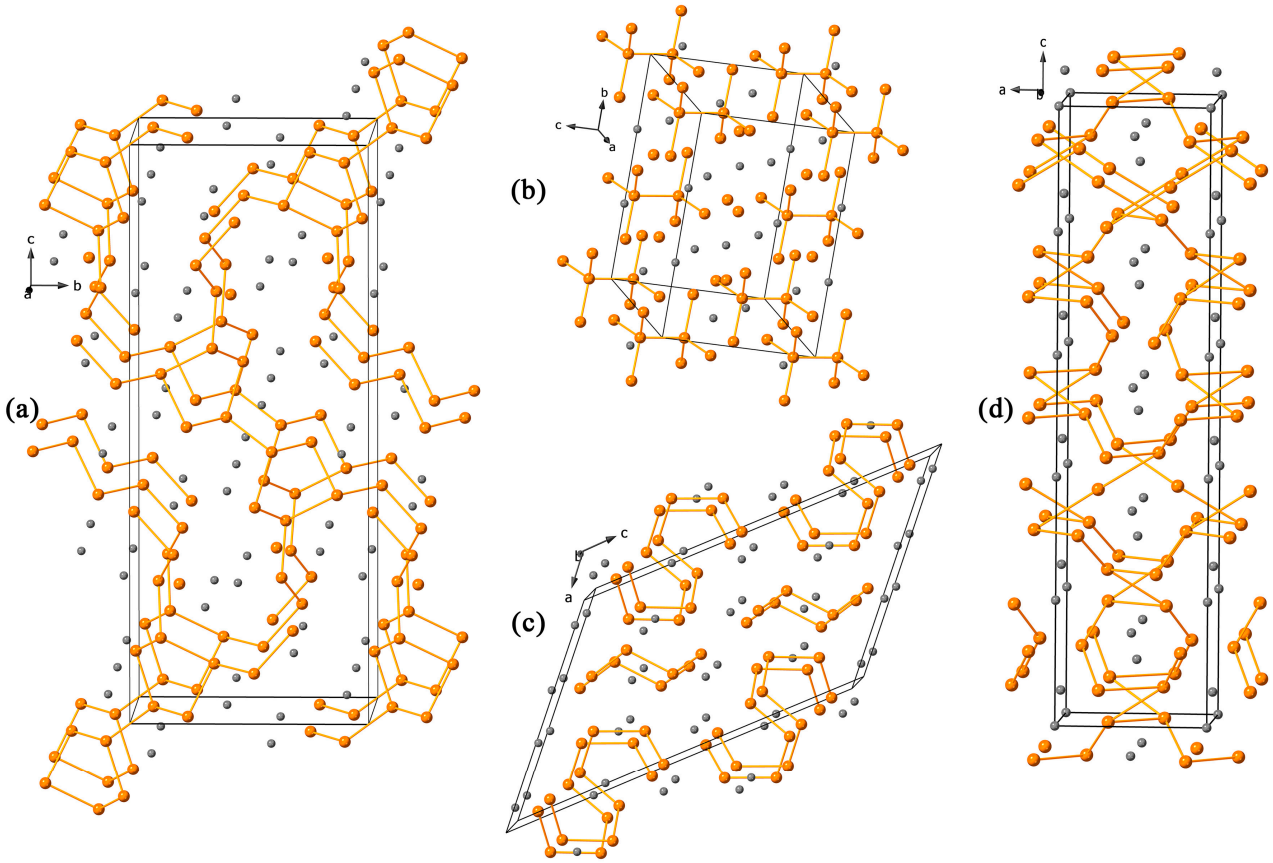


Figure A1. A schematic representation of four structure types, compositionally (**a**,**b**,**d**) and structurally (**c**) relevant to the title Ba_5Sb_8 phase. (**a**) In the Cs_5Sb_8 structure type, Sb atoms are arranged into five-membered rings linked via short Sb chains. (**b**) In the Ca_5P_8 structure type, the anionic substructure is described as isolated P_8^{10-} anions isostructural to the staggered conformation of ethane. (**c**) The anionic substructure of Ca_2As_3 consists of four- and eight-membered chains composed of As atoms. (**d**) A three-dimensional network of Sb atoms within the $[Ti,Zr]_5Sb_8$ structure type.

References

1. Schäfer, H.; Eisenmann, B.; Müller, W. Zintl Phases: Transitions between Metallic and Ionic Bonding. *Angew. Chem. Int. Ed. Eng.* **1973**, *12*, 694–712. [CrossRef]
2. Nesper, R. The Zintl-Klemm Concept—A Historical Survey. *Z. Anorg. Allg. Chem.* **2014**, *640*, 2639–2648. [CrossRef]
3. Liu, K.F.; Xia, S.-Q. Recent Progresses on Thermoelectric Zintl Phases: Structures, Materials and Optimization. *J. Solid State Chem.* **2019**, *270*, 252–264. [CrossRef]
4. Hodge, K.; Goldberger, J. Alkyne Hydrogenation Catalysis across a Family of Ga/In Layered Zintl Phases. *ACS Appl. Mater. Interfaces* **2021**, *13*, 52152–52159. [CrossRef] [PubMed]
5. Brehm, J.A. Predicted Bulk Photovoltaic Effect in Hydrogenated Zintl Compounds. *J. Mater. Chem C* **2018**, *6*, 1470–1475. [CrossRef]
6. Park, J.; Han, J.; Gim, J.; Garcia, J.; Iddir, H.; Ahmed, S.; Xu, G.L.; Amine, K.; Johnson, C.; Jung, Y.; et al. Evidence of Zintl Intermediate Phase and Its Impacts on Li and Na Storage Performance of Pb-Based Alloying Anodes. *Chem. Mater.* **2023**, *35*, 4171–4180. [CrossRef]
7. Ogunbunmi, M.O.; Bobev, S. Exploiting the Fraternal Twin Nature of Thermoelectrics and Topological Insulators in Zintl Phases as a Tool for Engineering New Efficient Thermoelectric Generators. *J. Mater. Chem. C* **2023**, *11*, 8337–8357. [CrossRef]
8. Baranets, S.; Ovchinnikov, A.; Bobev, S. Structural Diversity of the Zintl Pnictides with Rare-Earth Metals. In *Handbook on the Physics and Chemistry of Rare Earths*; Elsevier: Amsterdam, The Netherlands, 2021; pp. 227–324.
9. Kauzlarich, S. Zintl Phases: From Curiosities to Impactful Materials. *Chem. Mater.* **2023**, *35*, 7355–7362. [CrossRef]
10. Dolyniuk, J.-A.; He, H.; Ivanov, A.S.; Boldyrev, A.I.; Bobev, S.; Kovnir, K. Ba and Sr Binary Phosphides: Synthesis, Crystal Structures, and Bonding Analysis. *Inorg. Chem.* **2015**, *54*, 8608–8616. [CrossRef]

11. Baranets, S.; Ovchinnikov, A.; Samarakoon, S.M.G.K.; Bobev, S. Synthesis, Crystal and Electronic Structure of the Zintl Phase $Ba_{16}Sb_{11}$. A Case Study Uncovering Greater Structural Complexity via Monoclinic Distortion of the Tetragonal $Ca_{16}Sb_{11}$ Structure Type. *Z. Anorg. Allg. Chem.* **2023**, *649*, e202300148. [CrossRef]
12. Hoffmann, A.; Hlukhyy, V.; Fässler, T. Crystal Structure of undecacalcium decaarsenide, $Ca_{11}As_{10}$. *Z. Kristallogr.—New Cryst. Struct.* **2023**, *238*, 1–3. [CrossRef]
13. Eisenmann, B.; Jordan, H.; Schäfer, H. Ba_2Sb_3, Eine Neue Zintlphase Mit Sb_6-Ketten/On Ba_2Sb_3, a New Zintl Phase with Sb_6 -Chains. *Z. Naturforsch. B* **1985**, *40*, 1603–1606. [CrossRef]
14. Derrien, G.; Monconduit, L.; Tillard, M.; Belin, C. Pentabarium Tetraantimonide, β-Ba_5Sb_4: A More Symmetrical Arrangement for the Ba_5Sb_4 Compound. *Acta Crystallogr. C* **1999**, *55*, 1044–1046. [CrossRef]
15. Emmerling, F.; Längin, N.; Pickhard, F.; Wendorff, M.; Röhr, C. Verbindungen Mit Pentelid-Hanteln M_2: $A^{I}_{II}M_6$ Und $A^{II}{}_{11}M_{10}$ (A = Rb, Cs, Ba; M = Sb, Bi)/Compounds with Pentelide Dumbbells M_2: $A^{I}{}_{11}M_6$ and $A^{II}{}_{11}M_{10}$ (A = Rb, Cs, Ba; M = Sb, Bi). *Z. Naturforsch. B* **2004**, *59*, 7–16. [CrossRef]
16. Eisenmann, B.; Gieck, C.; Rößler, U. Crystal Structure of Barium Diantimonide, $BaSb_2$. *Z. Kristallogr.—New Cryst. Struct.* **2001**, *216*, 36. [CrossRef]
17. Deller, K.; Eisenmann, B. $BaSb_3$, Ein Antimonid Mit Einem Zweidimensional Unendlichen $[Sb_3{}^{2-}]_n$-Polyanion/$BaSb_3$, an Antimonide with an Infinite Two Dimensional $[Sb_3{}^{2-}]_n$—Anion. *Z. Naturforsch. B* **1978**, *33*, 676–677. [CrossRef]
18. Ovchinnikov, A.; Bobev, S. Exploration of Multi-Component Vanadium and Titanium Pnictides Using Flux Growth and Conventional High-Temperature Methods. *Front. Chem.* **2020**, *7*, 909. [CrossRef] [PubMed]
19. Ovchinnikov, A.; Bobev, S. Bismuth as a Reactive Solvent in the Synthesis of Multicomponent Transition-Metal-Bearing Bismuthides. *Inorg. Chem.* **2020**, *59*, 3459–3470. [CrossRef]
20. Cicirello, G.; Wang, M.; Sam, Q.P.; Hart, J.L.; Williams, N.L.; Yin, H.; Cha, J.J.; Wang, J. Two-Dimensional Violet Phosphorus P_{11}: A Large Band Gap Phosphorus Allotrope. *J. Am. Chem. Soc.* **2023**, *145*, 8218–8230. [CrossRef]
21. Todorov, I.; Young Chung, D.; Ye, L.; Freeman, A.J.; Kanatzidis, M.G. Synthesis, Structure and Charge Transport Properties of $Yb_5Al_2Sb_6$: A Zintl Phase with Incomplete Electron Transfer. *Inorg. Chem.* **2009**, *48*, 4768–4776. [CrossRef]
22. Hadenfeldt, C.; Bartels, F. Pentacalciumhexaphosphahypodiphosphat, Ca_5P_8: Eine Verbindung Mit Isolierten Anionen $P_8{}^{10-}$ Mit Der Gestaffelten Konformation von Ethan. *Z. Anorg. Allg. Chem.* **1994**, *620*, 1247–1252. [CrossRef]
23. Emmerling, F.; Hirschle, C.; Röhr, C. Cs_5Sb_8 Und β-CsSb: Zwei Neue Binäre Zintl-Phasen. *Z. Anorg. Allg. Chem.* **2002**, *628*, 559–563. [CrossRef]
24. Kleinke, H. A Three-Dimensional Extended Sb Network in the Metallic Antimonides $(M',Ti)_5Sb_8$ (M′ = Zr, Hf, Nb, Mo). *Inorg. Chem.* **2001**, *40*, 95–100. [CrossRef] [PubMed]
25. Tavassoli, A.; Grytsiv, A.; Failamani, F.; Rogl, G.; Puchegger, S.; Müller, H.; Broz, P.; Zelenka, F.; Macciò, D.; Saccone, A.; et al. Constitution of the Binary M-Sb Systems (M = Ti, Zr, Hf) and Physical Properties of MSb_2. *Intermetallics* **2018**, *94*, 119–132. [CrossRef]
26. Cordero, B.; Gómez, V.; Platero-Prats, A.E.; Revés, M.; Echeverría, J.; Cremades, E.; Barragán, F.; Alvarez, S. Covalent Radii Revisited. *Dalton Trans.* **2008**, 2832–2838. [CrossRef]
27. Goicoechea, J.M. Homoatomic Polyanions of the Early P-Block Elements. In *Clusters—Contemporary Insight in Structure and Bonding. Structure and Bonding*; Dehnen, S., Ed.; Springer: Cham, Switzerland, 2016; pp. 63–97.
28. Deller, K.; Eisenmann, B. Die Kristallstruktur Des Ca_2As_3. *Z. Naturforsch. B* **1976**, *31*, 1023–1027. [CrossRef]
29. Wang, Y.; Calvert, L.D.; Smart, M.L.; Taylor, J.B.; Gabe, E.J. The Structure of Trieuropium Tetraarsenide. *Acta Crystallogr. B* **1979**, *35*, 2186–2188. [CrossRef]
30. von Schnering, H.-G.; Wittmann, M.; Sommer, D. Eu_3P_4, Sr_3P_4 Und Ba_3P_4, Polyphosphide Mit $P_4{}^{6-}$-Ketten in Einer α-$ThSi_2$-Defektstruktur. *Z. Anorg. Allg. Chem.* **1984**, *510*, 61–71. [CrossRef]
31. Saal, J.E.; Kirklin, S.; Aykol, M.; Meredig, B.; Wolverton, C. Materials Design and Discovery with High-Throughput Density Functional Theory: The Open Quantum Materials Database (OQMD). *JOM* **2013**, *65*, 1501–1509. [CrossRef]
32. Wang, H.-C.; Botti, S.; Marques, M.A.L. Predicting Stable Crystalline Compounds Using Chemical Similarity. *NPJ Comput. Mater.* **2021**, *7*, 12. [CrossRef]
33. Pauling, L. *The Nature of the Chemical Bond and the Structure of Molecules and Crystals: An Introduction to Modern Structural Chemistry*, 3rd ed.; Cornell Univ. Press: Ithaca, NY, USA, 2000; ISBN 978-0-8014-0333-0.
34. Brown, S.R.; Kauzlarich, S.M.; Gascoin, F.; Snyder, G.J. $Yb_{14}MnSb_{11}$: New High Efficiency Thermoelectric Material for Power Generation. *Chem. Mater.* **2006**, *18*, 1873–1877. [CrossRef]
35. Baranets, S.; Bobev, S. From the Ternary Phase $Ca_{14}Zn_{1+\delta}Sb_{11}$ ($\delta \approx 0.4$) to the Quaternary Solid Solutions $Ca_{14-x}RE_xZnSb_{11}$ (*RE* = La–Nd, Sm, Gd, $x \approx 0.9$). A Tale of Electron Doping via Rare-Earth Metal Substitutions and the Concomitaln Structural Transformations. *Inorg. Chem.* **2019**, *58*, 8506–8516. [CrossRef] [PubMed]
36. Zevalkink, A.; Takagiwa, Y.; Kitahara, K.; Kimura, K.; Snyder, G.J. Thermoelectric Properties and Electronic Structure of the Zintl Phase $Sr_5Al_2Sb_6$. *Dalton Trans.* **2014**, *43*, 4720–4725. [CrossRef] [PubMed]
37. Hu, Y.; Wang, J.; Kawamura, A.; Kovnir, K.; Kauzlarich, S. $Yb_{14}MgSb_{11}$ and $Ca_{14}MgSb_{11}$—New Mg-Containing Zintl Compounds and Their Structures, Bonding, and Thermoelectric Properties. *Chem. Mater.* **2015**, *27*, 343–351. [CrossRef]
38. Liu, K.; Liu, Q.; Wang, Q.; Su, Y.; Zhou, S.; Liu, X.-C.; Xia, S.-Q. Cation Substitution and Size Effects in Ca_2ZnSb_2 and Yb_2MnSb_2: Crystal and Electronic Structures and Thermoelectric Properties. *Inorg. Chem.* **2023**, *62*, 7333–7341. [CrossRef]

39. *SAINT*; Bruker AXS Inc.: Madison, WI, USA, 2014.
40. *SADABS*; Bruker AXS Inc.: Madison, WI, USA, 2014.
41. Sheldrick, G.M. *SHELXT*—Integrated Space-Group and Crystal-Structure Determination. *Acta Crystallogr. A* **2015**, *71*, 3–8. [CrossRef]
42. Sheldrick, G.M. Crystal Structure Refinement with *SHELXL*. *Acta Crystallogr. C* **2015**, *71*, 3–8. [CrossRef]
43. Dolomanov, O.V.; Bourhis, L.J.; Gildea, R.J.; Howard, J.A.K.; Puschmann, H. OLEX2: A Complete Structure Solution, Refinement and Analysis Program. *J. Appl. Crystallogr.* **2009**, *42*, 339–341. [CrossRef]
44. Gelato, L.M.; Parthé, E. STRUCTURE TIDY—A Computer Program to Standardize Crystal Structure Data. *J. Appl. Crystallogr.* **1987**, *20*, 139–143. [CrossRef]
45. Jepsen, O.; Andersen, O.K. The Stuttgart TB-LMTO Program, Version 47, Stuttgard, Germany, 2000. Available online: https://www2.fkf.mpg.de/andersen/LMTODOC/LMTODOC.html (accessed on 18 December 2023).
46. von Barth, U.; Hedin, L. A Local Exchange-Correlation Potential for the Spin Polarized Case: I. *J. Phys. C Solid State Phys.* **1972**, *5*, 1629–1642. [CrossRef]
47. Steinberg, S.; Dronskowski, R. The Crystal Orbital Hamilton Population (COHP) Method as a Tool to Visualize and Analyze Chemical Bonding in Intermetallic Compounds. *Crystals* **2018**, *8*, 225. [CrossRef]

Disclaimer/Publisher's Note: The statements, opinions and data contained in all publications are solely those of the individual author(s) and contributor(s) and not of MDPI and/or the editor(s). MDPI and/or the editor(s) disclaim responsibility for any injury to people or property resulting from any ideas, methods, instructions or products referred to in the content.